ACS NANOSCIENCE Au
AN OPEN ACCESS JOURNAL OF THE AMERICAN CHEMICAL SOCIETY

pubs.acs.org/nanoau
Article

Leveraging Tunable Nanoparticle Surface Functionalization to Alter Cellular Migration

Maxwell G. Tetrick and Catherine J. Murphy*

Cite This: ACS Nanosci. Au 2024, 4, 205−215
Read Online

ABSTRACT: Gold nanoparticles (AuNPs) are a promising platform for biomedical applications including therapeutics, imaging, and drug delivery. While much of the literature surrounding the introduction of AuNPs into cellular systems focuses on uptake and cytotoxicity, less is understood about how AuNPs can indirectly affect cells via interactions with the extracellular environment. Previous work has shown that the monocytic cell line THP-1's ability to undergo chemotaxis in response to a gradient of monocyte chemoattractant protein 1 (MCP-1) was compromised by extracellular polysulfonated AuNPs, presumably by binding to MCP-1 with some preference over other proteins in the media. The hypothesis to be explored in this work is that the degree of sulfonation of the surface would therefore be correlated with the ability of AuNPs to interrupt chemotaxis. Highly sulfonated poly(styrenesulfonate)-coated AuNPs caused strong inhibition of THP-1 chemotaxis; by reducing the degree of sulfonation on the AuNP surface with copolymers [poly(styrenesulfonate-*co*-maleate) of different compositions], it was found that medium and low sulfonation levels caused weak to no inhibition, respectively. Small, rigid molecular sulfonate surfaces were relatively ineffective at chemotaxis inhibition. Unusually, free poly(styrenesulfonate) caused a dose-dependent reversal of THP-1 cell migration: at low concentrations, free poly(styrenesulfonate) significantly inhibited MCP-1-induced chemotaxis. However, at high concentrations, free poly(styrenesulfonate) acted as a chemorepellent, causing a reversal in the cell migration direction.

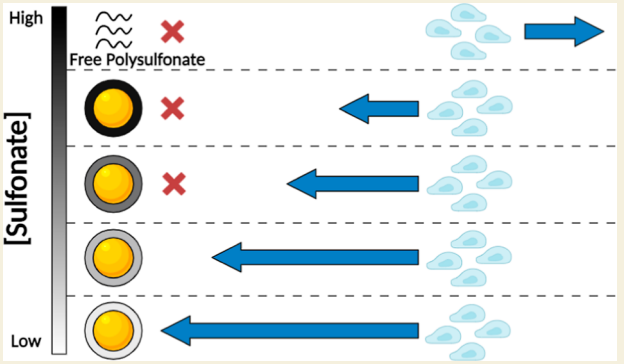

KEYWORDS: *chemorepellent, chemotaxis, gold nanoparticles, protein adsorption, sulfonation, surface chemistry*

Due to their size- and shape-dependent optical properties, gold nanoparticles (AuNPs) have drawn increasing interest for their potential use in biomedical applications; AuNPs are being studied for use as therapeutics, imaging agents, drug delivery systems, and diagnostics.[1−11] However, the impact of introducing AuNPs into biological systems has yet to be fully characterized.[12] Numerous studies have examined how altering various properties of AuNPs such as charge, surface chemistry, shape, and size affect AuNP-cell interactions.[13−21] Previous work has shown that cellular uptake during chronic, long-term AuNP exposure is largely dependent on AuNP surface chemistry; moreover, surface chemistry-dependent changes in gene expression were observed following acute, low-dose AuNP exposure, highlighting the impact of AuNP surface chemistry on the biological response.[20] Similarly, further studies have shown that changing AuNP surface functionalization alters the adsorption of serum proteins to the AuNP surface, which subsequently impacts interactions with cell membranes.[22−26]

Although the existing AuNP-bio interaction literature is largely focused on the direct interactions between AuNPs and cells (such as uptake, cytotoxicity, and gene expression), it has also been observed that AuNPs can influence cell behavior indirectly by modifying the local microenvironment. Recent work has shown that AuNPs can disrupt cross talk between cells and alter the mechanical and chemical properties of the extracellular matrix (ECM).[27−34] This disruption can extend to cellular behaviors such as chemotaxis, the directed migration of cells in response to a chemical gradient. Chemotaxis is responsible for infection and would healing in humans and can be greatly affected by changes in the ECM.[35−38] Dysfunctions in cellular chemotaxis have been implicated in a variety of health problems such as chronic obstructive pulmonary disease, cystic fibrosis, infertility, and cancer metastasis.[36,39−42]

Previously, it was found that AuNPs in the extracellular environment of the human monocytic cell line THP-1 caused significant inhibition of chemotaxis that had been generated by ng/mL amounts of monocyte chemoattractant protein 1 (MCP-1).[43] MCP-1 is a 13 kDa member of the chemokine family that bears a net positive charge at pH 7.4.[44] It was found

Received: November 5, 2023
Revised: January 26, 2024
Accepted: January 30, 2024
Published: February 14, 2024

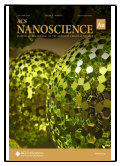

https://doi.org/10.1021/acsnanoscienceau.3c00055
ACS Nanosci. Au 2024, 4, 205−215

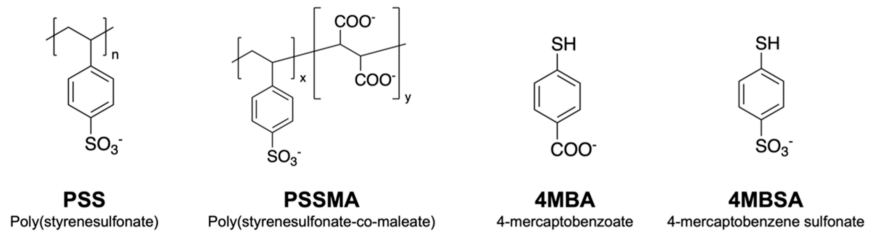

Figure 1. Library of AuNP surface coatings with their abbreviations. PSSMA is a block copolymer that was used in two x/y ratios, 3:1 and 1:1.

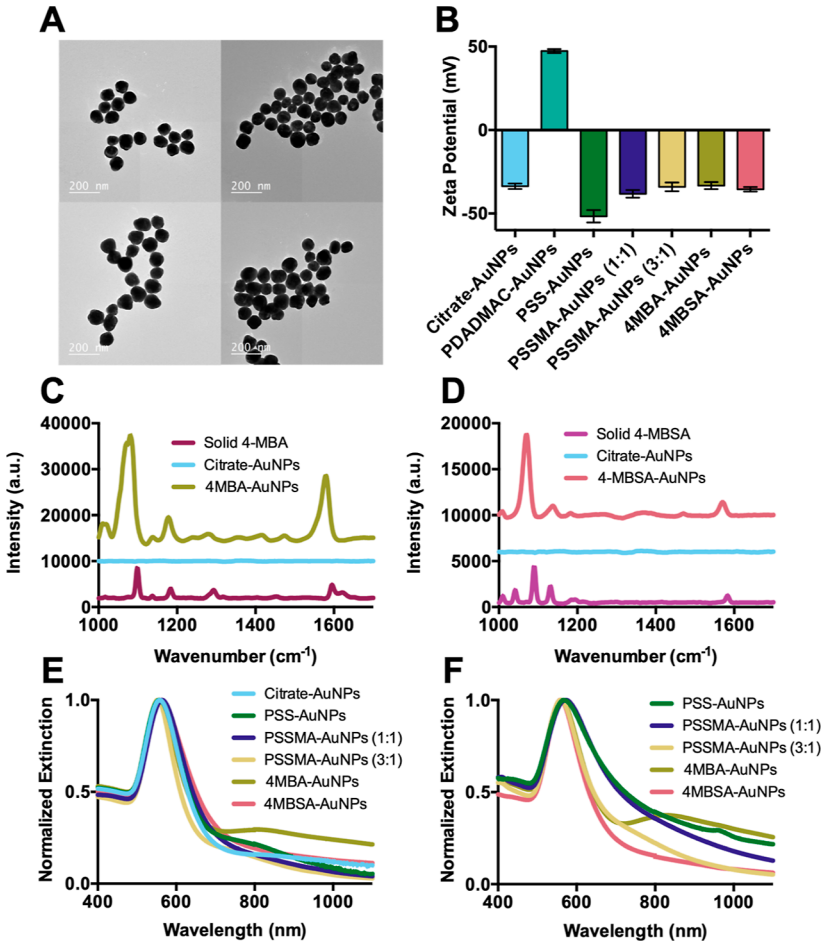

Figure 2. (a) Representative TEM images of 90 nm citrate-AuNPs (average diameter: 92 ± 11 nm). (b) Zeta potential measurements of functionalized AuNPs, confirming success of polyelectrolyte wrapping, for initial citrate, intermediate PDADMAC cationic layer (see Materials and Methods), and final PSS or PSSMA polyelectrolytes; and for small-molecule MBA/MBSA functionalization directly from the citrate precursor. Error bars represent one standard deviation from the mean. (c,d) Surface-enhanced Raman spectra of (c) 4MBA-AuNPs and (d) 4MBSA-AuNPs compared to precursor citrate-AuNPs and solid free ligands, demonstrating surface functionalization. (e) Extinction spectra of AuNPs in water as a function of terminal surface chemistry. Extinction at ∼800 nm is indicative of mild aggregation. (f) Extinction spectra of the same AuNPs as in (e) after incubating in RPMI cell media for 24 h.

that negatively charged poly(styrenesulfonate) (PSS)-coated AuNPs reduced THP-1 cell migration by over 50% as measured by total cell displacement. Upon further investigation, PSS-AuNPs adsorbed roughly 10% of MCP-1 in solution,[43] enough to cause a significant decrease in directed cell migration due to the narrow concentration ranges that govern chemotaxis.[45−48] Interestingly, citrate-AuNPs (also negatively charged) had minimal adsorption of MCP-1 and limited impact on chemotaxis, indicating that electrostatic interactions alone do not predict NP-protein binding.[43] Indeed, related work on the native MCP-1 receptor CCR2 shows that tyrosine sulfation in the active site increases the affinity of MCP-1 for the MCP-1 receptor.[49−51]

In this work, tunable control over THP-1 chemotaxis is demonstrated by altering the degree of sulfonation of the AuNP surfaces. A small library of AuNPs bearing various ligands with different degrees of sulfonation, both flexible and rigid (Figure 1), was created with the goal of furthering understanding of how the NP surface presentation of ligands affects protein binding with subsequent indirect effects on cell behavior.

https://doi.org/10.1021/acsnanoscienceau.3c00055
ACS Nanosci. Au 2024, 4, 205−215

2. RESULTS AND DISCUSSION

Citrate-capped AuNPs approximately 90 nm in diameter were synthesized using the seed-mediated hydroquinone-reduction method,[52] and their size and shape were characterized with transmission electron microscopy (Figure 2a). Citrate-AuNPs were functionalized using either the polyelectrolyte layer-by-layer wrapping approach[53] for PSS-AuNPs, PSSMA-AuNPs (1:1), and PSSMA-AuNPs (3:1) or using the thiol displacement approach for 4MBA-AuNPs and 4MBSA-AuNPs. By functionalizing AuNPs with alternating positive and negative polyelectrolytes, a reversal of the AuNP surface charge upon adsorption of each subsequent layer is expected. The surface charges of all functionalized AuNPs were characterized with zeta potential measurements. Success of polyelectrolyte wrapping was monitored by observing a flip in charge from the negative citrate coating to the positive poly(diallyldimethylammonium chloride) (PDADMAC) coating back to negative for the final anionic polyelectrolyte layer (Figure 2b). Confirmation of small-molecule functionalization was determined by monitoring for the presence of characteristic peaks using surface-enhanced Raman spectroscopy (Figure 2c,d).

Extinction spectra of all AuNPs were taken to ensure an appropriate surface plasmon resonance for a 90 nm AuNP and that aggregated species are not predominant in solution (Figure 2e). Figure 2e shows that all AuNPs exhibit an expected extinction maximum around 558 nm. Additionally, while there is some slight aggregation present in the 4MBA-AuNPs (as evidenced by increased absorption above 800 nm), all functionalized AuNPs were largely free of aggregated species (Figure 2e). AuNP colloidal stability in cell culture media was assessed after 24 h (Figure 2f). All AuNPs showed fair colloidal stability with expected peak broadening and upward baseline shift due to the high protein and high ionic strength environment (Figure 2f).

Polyelectrolyte wrapping with polymers containing different sulfonate compositions will presumably lead to different degrees of sulfonation on the AuNP surface. In order to experimentally estimate the degree of sulfonation of the functionalized AuNPs, colloidal stability at increasing ionic strengths was measured. First, AuNP solutions were adjusted to pH 3, neutralizing carboxylic acids (pK_a ~5) present on the AuNP surface while retaining a negative charge on sulfonates ($pK_a < 0$). By decreasing the solution pH, it is ensured that the colloidal stability of the AuNPs is due to electrostatic repulsion of sulfonate functional groups, and carboxylate contributions are eliminated. Next, aggregation was induced by adding NaCl solutions of increasing concentrations to the AuNPs. Relative aggregation states of the AuNP library were compared by monitoring the decrease in the absorbance of the 560 nm plasmon peak as the ionic strength increased (Figure 3). As expected, 4MBA-AuNPs that bear only carboxylic acid surface groups aggregated immediately after being adjusted to pH 3. The four remaining AuNPs largely remained stable up to 0.023 M NaCl which caused a significant reduction in measured 560 nm extinction for all AuNPs (Figure 3). Table 1 shows the relative stability values of AuNPs in 0.023 M NaCl normalized to the "fully" sulfonated PSS-AuNPs. By comparison of relative aggregation states, relative sulfonate concentration on the AuNP surface can be estimated. A roughly 25 and 50% decrease in stability for PSSMA-AuNPs (3:1) and PSSMA-AuNPs (1:1), respectively, was expected compared to PSS-AuNPs due to the different molar ratios of styrenesulfonate in PSSMA. It was found that PSSMA-AuNPs (3:1) had 82% and PSSMA-AuNPs (1:1) had 64% relative extinction compared to PSS-AuNPs (Table 1). Additionally, 4MBSA-AuNPs had a 45% relative stability compared to PSS-AuNPs. Since the colloidal stability of the AuNPs is directly related to the concentration of surface sulfonates in this case, the AuNP library has relative sulfonate concentrations of 100, 82, 64, 45, and 0% for PSS, PSSMA (3:1), PSSMA (1:1), 4MBSA, and 4MBA, respectively.

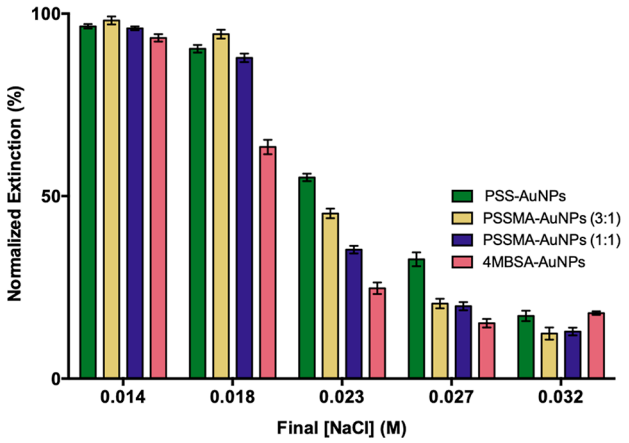

Figure 3. Comparison of the colloidal stability of AuNPs after the addition of increasing concentrations of NaCl as a function of terminal surface chemistry, at pH = 3.0. Bar heights represent mean AuNP extinction values at 560 nm normalized to their respective extinctions in 0 M NaCl. Error bars represent one standard deviation from the mean. All AuNP (0.04 nM, 100 μL) solutions were adjusted to pH 3 prior to the addition of 10 μL of NaCl (final concentration: 0−0.032 M NaCl, 0.036 nM AuNPs). 4MBA-AuNPs aggregated immediately after pH adjustment and are not included.

Table 1. Comparison of Extinction Values Relative to PSS-AuNPs in 0.023 M NaCl

AuNP surface coating	expected relative extinction (%)	measured relative extinction (%)	estimated degree of sulfonation (%)
PSS	100	100 ± 2	100
PSSMA (3:1)	75	82 ± 2	82
PSSMA (1:1)	50	64 ± 2	64
4MBSA		45 ± 3	45

2.1. Measuring Chemotaxis

In order to measure chemotaxis, THP-1 cells were suspended in a 1.5 mg/mL collagen matrix in the appropriate channel on the Ibidi chemotaxis μ-slide (Figure 4a). Each collagen matrix is surrounded by two reservoirs that can be filled with solutions of interest for various conditions (Figure 4a). For the positive control, one reservoir was filled with 50 ng/mL MCP-1 in RPMI cell media, while the other was filled with just RPMI, forming a chemoattractant gradient across the collagen matrix (Figure 4b). In the negative and balanced MCP-1 controls, both reservoirs were filled with either RPMI alone or 25 ng/mL MCP-1 in RPMI, respectively (Figure 4b), to confirm that cell migration in the positive control occurs due to the formation of a chemoattractant gradient. All AuNP conditions contained 0.02 nM AuNPs, 50 ng/mL MCP-1 in RPMI in one reservoir, and RPMI alone in the other (Figure 4b), allowing

https://doi.org/10.1021/acsnanoscienceau.3c00055
ACS Nanosci. Au 2024, 4, 205−215

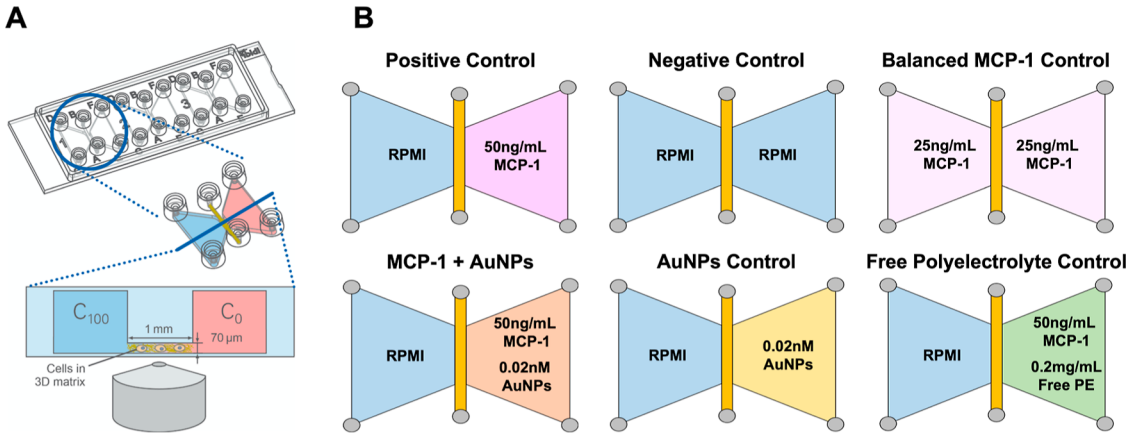

Figure 4. (a) Diagram of the Ibidi μ-slide for chemotaxis. Image courtesy of Ibidi GmbH.[55] (b) Slide setup for various experimental conditions. The positive control has the chemoattractant MCP-1 in media on one side of the cell channel with media alone on the other. The negative control has only media in both chambers. AuNP experiments are performed by the introduction of various NPs at the indicated concentration with the MCP-1 chemoattractant. AuNP controls do not include the MCP-1 chemoattractant. Free polyelectrolyte controls do include the MCP-1 chemoattractant.

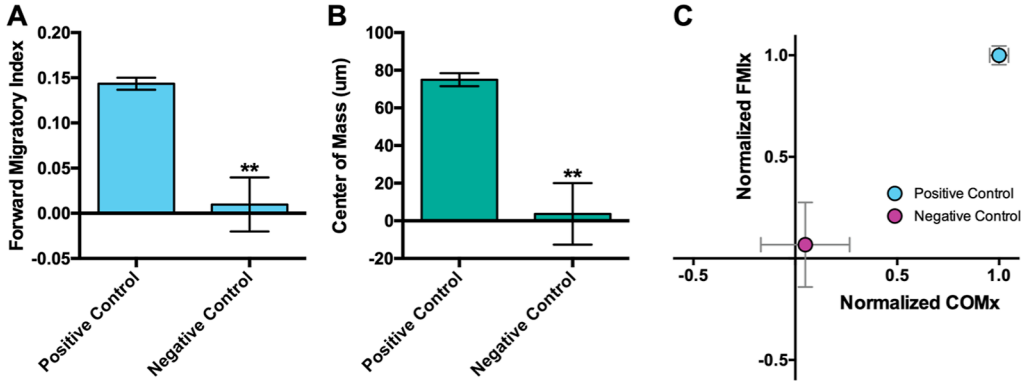

Figure 5. (a) Forward migratory index (x) and (b) center of mass (x) for positive (with MCP-1) and negative (no MCP-1) THP-1 chemotaxis controls. Bar heights represent mean values ($n \geq 6$). **$p < 0.01$, Dunnett's test. (c) FMI_x and COM_x of the negative control normalized to the positive control. Error bars represent the standard error of the mean. All MCP-1 concentrations were 50 ng/mL.

for the analysis of AuNP disruption of the chemoattractant gradient and subsequent reduction in THP-1 chemotaxis. Additionally, any potential intrinsic AuNP effect on cell migration was controlled by including AuNP controls that contained 0.02 nM AuNPs in RPMI in one reservoir and RPMI alone in the other (Figure 4b). Finally, the effects of the free polyelectrolyte coating—absent the AuNPs—were analyzed by the free polyelectrolyte condition containing 0.2 mg/mL polyelectrolyte, 50 ng/mL MCP-1 in RPMI in one reservoir, and just RPMI in the other reservoir (Figure 4b).

Cell migration was observed by imaging individual cells within the chemotaxis chambers on an optical microscope in the brightfield mode. Cells were imaged every 10 min for a period of 24 h, while temperature, humidity, and CO_2 levels were kept at standard incubation levels. Image analysis was conducted using FastTrack AI cell migration analysis software by MetaVi Laboratories. Cells were tracked and analyzed if they were recognized by FastTrack AI for more than 12 of the 24 h of experiment time and if they traveled a total distance of at least 100 μm, mimicking manual tracking parameters used previously.[43] Previous work has shown that these types of NPs do not impact THP-1 cell viability and are not taken up by THP-1 cells in these chemotaxis chambers to any appreciable extent.[43]

To quantify chemotaxis, two common measures of cell migration were used: forward migratory index (FMI) and center of mass (COM) (eqs 1 and 2).[54] In both equations, $x_{i,\mathrm{end}}$ represents the x-coordinate of the end point of a given cell, and n represents the total number of cells tracked. In eq 1, $d_{i,\mathrm{accum}}$ represents the total accumulated distance a given cell has traveled. FMI is a measure of the efficiency with which cells migrate, and COM measures the average cell displacement after 24 h. Both FMI and COM can be measured along the axis parallel (x) or perpendicular (y) to the chemoattractant gradient. However, for the purpose of this study, FMI and COM along the parallel X-axis (FMI_x and COM_x) are of primary interest. Differences in the FMI_x and COM_x across various experimental conditions indicate how the MCP-1 gradient and chemotaxis are disrupted in the presence of AuNPs. Analysis of perpendicular (y-axis) FMI and COM can be found in the Supporting Information (Figure S1).

$$\mathrm{FMI}_x = \frac{1}{n}\sum_{i=1}^{n}\frac{x_{i,\mathrm{end}}}{d_{i,\mathrm{accum}}} \tag{1}$$

$$\mathrm{COM}_x = \frac{1}{n}\sum_{i=1}^{n}\left(x_{i,\mathrm{end}}\right) \tag{2}$$

https://doi.org/10.1021/acsnanoscienceau.3c00055
ACS Nanosci. Au 2024, 4, 205−215

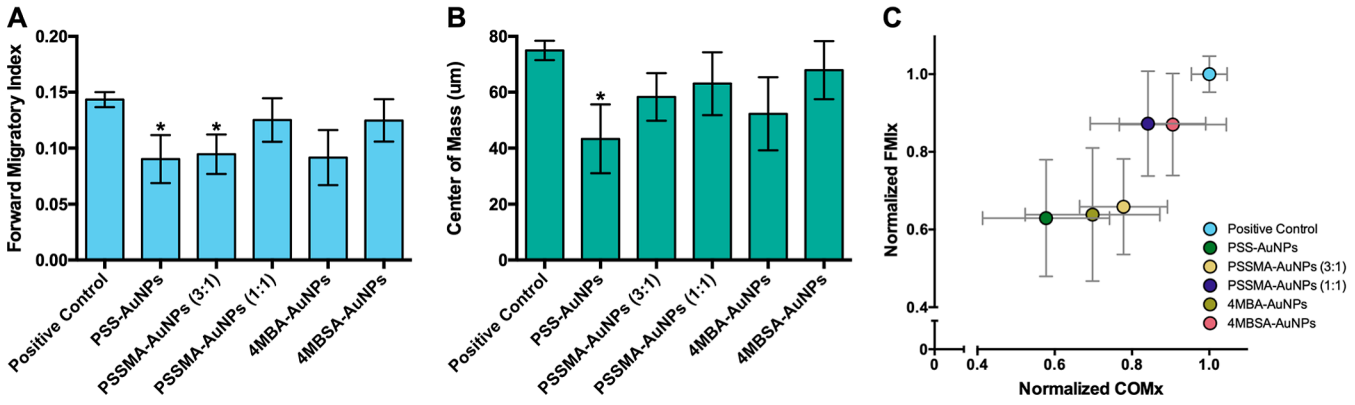

Figure 6. (a) Forward migratory index (x) and (b) center of mass (x) for various AuNP chemotaxis conditions, in which the indicated NPs (0.02 nM) were incubated with the MCP-1 chemoattractant (50 ng/mL). Bar heights represent mean values ($n \geq 6$). *$p < 0.05$, Dunnett's test. (c) FMI_x and COM_x of AuNP conditions normalized to the positive control. Error bars represent the standard error of the mean.

2.2. MCP-1 Induces Chemotaxis in THP-1 Cells

To evaluate the tunable AuNP inhibition of chemotaxis, an appropriate baseline is necessary to compare to various experimental conditions. Figure 5a,b shows the FMI_x and COM_x for the positive control. The positive control induced an average x-displacement (COM_x) of 75.0 ± 3.5 μm with an average FMI_x of 0.143 ± 0.007 (Figure 5a,b). To confirm that the positive control does in fact induce chemotaxis, COM_x and FMI_x were compared to that of the negative control. Figure 5a,b shows that the MCP-1 standard had a significantly higher average COM_x and FMI_x compared to the negative control which had a COM_x of 3.6 ± 16.3 μm and a FMI_x of 0.010 ± 0.030. The balanced MCP-1 control also showed nearly zero average cell displacement (data not shown), indicating that THP-1 cells experience chemotaxis in response to a chemoattractant gradient rather than ubiquitous chemoattractants in the environment. Plotting FMI_x and COM_x of the negative control normalized to the positive control shows that it is located near the origin (Figure 5c), further highlighting the lack of directional cell migration without MCP-1 in solution. Taken together, it is clear that the positive control induces chemotaxis in THP-1 cells and provides an appropriate baseline comparison for experimental conditions. Representative time-lapse videos of positive and negative controls are available in the Supporting Information (Movies S1 and S2).

2.3. AuNPs Enable Tunable Inhibition of Chemotaxis

The three polyelectrolyte-wrapped AuNPs [PSSMA (1:1), PSSMA (3:1), and PSS] were chosen for their increasing numbers of sulfonate groups in their polyelectrolyte surface coatings. Increased chemotaxis inhibition corresponding to an increased degree of sulfonation for the same surface area was expected, with the previously studied PSS-AuNPs causing the greatest effect on cell migration. Figure 6a,b shows the FMI_x and COM_x of various AuNP conditions compared to the benchmark positive control. Consistent with previous work,[43] it was found that PSS-AuNPs caused a significant decrease in both FMI_x and COM_x (Figure 6a,b). The PSS-AuNPs condition had an average FMI_x of 0.090 ± 0.022 and an average COM_x of 43.3 ± 12.3 μm, an approximately 40% decrease in both metrics compared to the positive control (Figure 6a,b). The PSSMA-AuNPs (3:1) similarly inhibited chemotaxis but to a lesser degree; FMI_x was significantly decreased (0.094 ± 0.018), and COM_x was reduced (58.3 ± 8.5 μm) but was not significantly different from the positive control (Figure 6a,b). Furthermore, PSSMA-AuNPs (1:1) showed no significant impact on either FMI_x or COM_x (0.125 ± 0.019 and 63.1 ± 11.2 μm, respectively) when compared to the positive control, supporting the notion that the presence of surface sulfonate groups drives chemotaxis disruption. By normalizing the polyelectrolyte-wrapped AuNP conditions to the positive control, the impact of the degree of sulfonation is more easily visualized (Figure 6c). Figure 6c emphasizes the strength of inhibition by showing that PSS-AuNPs are the farthest from the positive control and had the strongest influence on chemotaxis, followed by the weak inhibition of PSSMA-AuNPs (3:1), and no statistically significant inhibition of PSSMA-AuNPs (1:1).

In addition to the three polyelectrolyte-wrapped AuNPs, the effects of two small-molecule-functionalized AuNPs, 4MBA-AuNPs and 4MBSA-AuNPs, were analyzed. 4MBA and 4MBSA were chosen because of their chemical similarity to the monomer of PSS and their thiol group, allowing for ease of functionalization on the AuNP surface (Figure 1). Due to their low relative concentration of sulfonates (compared to other sulfonated AuNPs), 4MBSA-AuNPs were expected to have a limited impact on THP-1 chemotaxis (Table 1). 4MBA-AuNPs were similarly expected to minimally effect chemotaxis because of their lack of sulfonate groups. Moreover, due to the increased rigidity of small-molecule-coated AuNPs compared to the more flexible polyelectrolyte-wrapped AuNPs, it is expected that 4MBA- and 4MBSA-AuNPs will be less effective at adsorbing MCP-1. By restricting the conformation of sulfonate groups to the AuNP surface, it may be more challenging for AuNPs to adsorb MCP-1 in the correct orientation.

The 4MBSA-AuNPs indeed showed little chemotaxis inhibition with a FMI_x of 0.125 ± 0.019 and COM_x of 67.9 ± 10.4 μm (Figure 6a,b). Normalized to the positive control, it is apparent that 4MBSA-AuNPs had the least total impact on chemotaxis and were the most comparable to the positive control (Figure 6c). Additionally, upon visual inspection, 4MBA-AuNPs appear to cause a comparable reduction in FMI_x compared to PSS-AuNPs (Figure 6a). However, after statistical analysis using the standard $p = 0.05$ cutoff, it was determined that the 4MBA-AuMP data yields $p = 0.076$, and therefore is "insignificant", while the PSS-AuNP yields $p = 0.038$, and therefore is "significant". Figure S2 shows raw cell trajectories for interested readers. It should be noted that after 24 h of incubation in cell media, 4MBA-AuNPs experienced

https://doi.org/10.1021/acsnanoscienceau.3c00055
ACS Nanosci. Au 2024, 4, 205−215

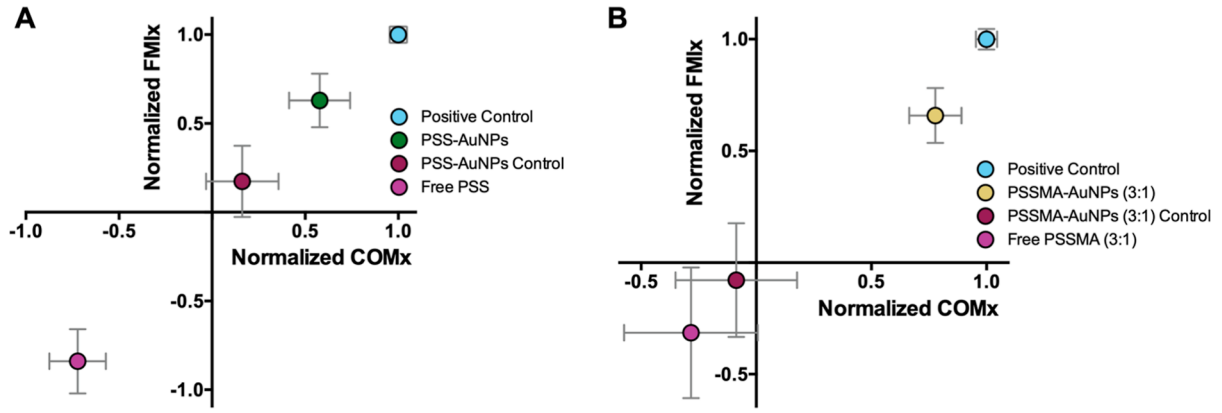

Figure 7. (a) FMI_x and COM_x of PSS-AuNPs (with MCP-1), PSS-AuNPs control (no MCP-1), and free PSS (with MCP-1) normalized to the positive control. (b) FMI_x and COM_x of PSSMA-AuNPs (3:1) (with MCP-1), PSSMA-AuNPs (3:1) control (no MCP-1), and free PSSMA (3:1) (with MCP-1) normalized to the positive control. Error bars represent the standard error of the mean. Concentrations are given in the text.

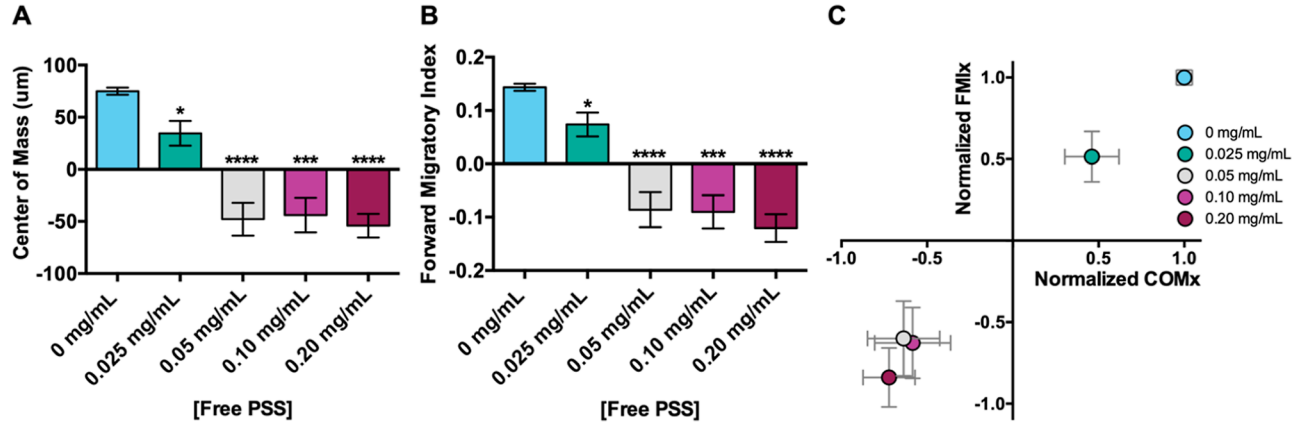

Figure 8. (a) Center of mass (x) and (b) forward migratory index (x) for THP-1 cells under various concentrations of free PSS. The positive control is considered 0 mg/mL PSS. All conditions contain 50 ng/mL MCP-1. Bar heights represent mean values ($n \geq 6$). *$p < 0.05$, ***$p < 0.001$, and ****$p < 0.0001$ Dunnett's test. (c) FMI_x and COM_x of various free PSS concentrations normalized to the positive control (0 mg/mL PSS) for THP-1 chemotaxis. Error bars represent the standard error of the mean.

the highest amount of aggregation compared to the other AuNPs used in this study (Figure 2f). Such aggregation may be a confounding factor in comparisons across NP surface chemistries.

To better understand the nature of the PSS-AuNPs and PSSMA-AuNPs (3:1) chemotaxis inhibition, both AuNPs were compared to a AuNP control and a free polyelectrolyte control. Figure 7 shows FMI_x and COM_x for the PSS-AuNPs and PSSMA-AuNPs (3:1) conditions and associated controls normalized to the positive control. When no MCP-1 is present, the PSS- and PSSMA-AuNPs (3:1) induce no chemotactic effect on their own; both controls resulted in near zero values for FMI_x and COM_x, indicating no directional cell migration (Figure 7a,b). The free PSSMA (3:1) control (containing 50 ng/mL MCP-1) yielded slightly negative, but near zero, values for both FMI_x and COM_x, indicating that the free polymer without the AuNP support can fully inhibit any chemotactic behavior induced by MCP-1 in solution (Figure 7b). Notably, the free PSS control caused a reversal in the THP-1 migration direction. As evidenced by the large negative values of FMI_x and COM_x, the free PSS control caused THP-1 cells to migrate away from the reservoir containing 0.2 mg/mL free PSS and 50 ng/mL MCP-1 (Figure 7a). Previously, 0.2 mg/mL free PSS resulted in modest, near zero values for FMI_x and COM_x in initial trials ($n = 2$) and was not explored further at that time.[43] In this study, initial trials with free PSS showed a strong chemorepellent effect which was probed with additional replicates ($n = 9$).[43] The current results suggest that the free PSS overcomes the chemoattraction caused by MCP-1 in solution and acts as a chemorepellent. Representative cell migration trajectory plots of all experimental conditions can be found in the Supporting Information (Figure S2).

2.4. Free PSS Causes Dose-Dependent Reversal of Cell Migration

To probe the chemorepellent effect of free PSS further, the response of THP-1 cells to a range of free PSS concentrations while keeping the concentration of the chemoattractant consistent (50 ng/mL MCP-1) was analyzed. Figure 8a,b shows the COM_x and FMI_x of various concentrations of free PSS compared to the positive control (50 ng/mL MCP-1, 0 mg/mL PSS). Even at the lowest concentration tested (0.025 mg/mL), free PSS more strongly inhibited chemotaxis than PSS-AuNPs for both FMI_x and COM_x (Figure 8a,b). Interestingly, by doubling the free PSS concentration to 0.05 mg/mL, a complete reversal in cell migration direction was observed, indicating that PSS fully overcomes the chemoattractant force of MCP-1 and acts as a chemorepellent to THP-1 cells. It should be noted that many chemotaxis assays rely on cell migration in a Boyden chamber, which would not

https://doi.org/10.1021/acsnanoscienceau.3c00055
ACS Nanosci. Au 2024, 4, 205−215

uncover any cells moving in the opposite direction of a chemical gradient, which is an advantage of the present chemotaxis setup. The magnitude of the chemorepellent effect of free PSS remained relatively unchanged even as the concentration of free PSS was further increased (Figure 8a,b). Figure 8c shows the FMI_x and COM_x of each experimental condition normalized to the positive control. At the highest concentration tested (0.2 mg/mL), the magnitude of PSS repellence is nearly the same as the attractive force of the MCP-1 positive control (Figure 8c), and caused 74 of the 110 cells tracked to move in the negative x-direction.

It was hypothesized that the chemorepellent activity of free PSS could be caused by the polymer altering the properties of the collagen matrix. Previous work has shown that by incorporating PSS- and other sulfated-AuNPs into type I collagen, mechanical stiffness, and morphology are altered,[33,56] which can impact cell migration. The elastic modulus of collagen that had been incubated for 24 h in RPMI cell media (control) was tested and compared to collagen incubated in RPMI cell media containing 0.2 mg/mL PSS, mimicking chemotaxis assay conditions. However, there was no difference between the elastic modulus of the control collagen (485 ± 205 Pa, n = 3) compared to PSS-treated collagen (502 ± 188 Pa, n = 3), indicating that mechanical disruption is likely not the cause of PSS repellence. Thus, at the present time, the root cause for this unusual chemical behavior is unknown and requires further study.

Free PSS[57] and PSS-coated NPs[43,57−59] have previously been shown to be nontoxic to various mammalian and bacterial cell lines, with some cells experiencing enhanced migration when directly exposed to PSS-AuNPs.[59] However, work using heparan sulfate (HS) as a chemokine inhibitor could help explain the unexpected chemorepulsion activity of PSS. HS is a highly sulfated, long-chain polysaccharide that is an essential cofactor in the binding and activation of cell surface chemokine receptors.[60−62] Recently, there has been interest in using HS mimetics to reduce inflammation and cancer metastasis by regulating chemokine activity.[61,63] Two HS mimetics (both highly sulfated tetrasaccharides) showed strong binding to MCP-1.[64,65] Both HS mimetics reduced breast cancer cell proliferation and inhibited MCP-1 induced chemotaxis.[64,65] Researchers performed Boyden chamber migration assays to compare MCF-7 cell migration in the presence of no chemoattractant (negative control), only chemoattractant (positive control), and chemoattractant plus HS mimetic (treatment). Notably, HS mimetics not only completely masked the chemoattractant-induced migration but caused fewer cells to migrate in the treatment condition than in the negative control containing no chemoattractant, similar to the effect observed in this work.[64,65] While the cause of this apparent HS mimetic chemorepellent effect is not further explored, it is suspected that a similar phenomenon could be occurring in the current system due to the chemical similarity of the highly sulfated polyelectrolyte PSS to the HS mimetics. Future work examining the interactions between highly sulfated polyelectrolytes (such as PSS, HS, and HS mimetics) and cell surface receptors will provide valuable insights into the mechanism of chemorepulsion of these molecules.

2.5. Free PSS vs PSS-AuNPs

In this study, PSS-AuNPs and the free PSS polymer resulted in a significant inhibition of THP-1 chemotaxis. Free PSS concentrations (0.2 mg/mL) estimated to be representative of the concentration of PSS on the AuNP surface (for 0.02 nM PSS-AuNPs) resulted in a cellular response drastically different from that of PSS bound to NPs. It has been well-established that upon interacting with an oppositely charged nanoparticle surface, highly charged, flexible polymers—like PSS[66]—adopt a fully wrapped conformation around the nanoparticle surface.[67,68] Such wrapping can alter the molecular display and restrict the accessibility of sulfonate groups thought to interact with MCP-1. Moreover, with limited conformational freedom, it is likely that PSS adsorbed on the AuNP surface has more difficulty interacting with the appropriate regions of MCP-1 compared to that of the flexible free polymer.

Although free PSS resulted in more extreme inhibition (and reversal) of THP-1 chemotaxis than PSS-AuNPs in this application, it is important to note the benefit of NPs for cellular intervention. PSS modification has been shown previously to enhance endothelial cell uptake and targeting capability of NPs, but the incorporation of free PSS in solution causes inhibition of NP uptake.[69] Moreover, peptide vaccine-conjugated AuNPs have been shown to more effectively deliver vaccine payload to dendritic cells and stimulate lymphocytes than free peptide vaccines alone.[70] It is always recommended to compare free ligands to nanoparticle-bound ligands when undertaking nanobio experiments; in some cases, the free ligand may produce very different results compared to the NP-bound ligands.

3. CONCLUSIONS

Here, tunable control over cellular chemotaxis by altering the surface chemistry of the AuNPs was demonstrated. It was hypothesized that increased THP-1 chemotaxis inhibition would be observed with increasing degrees of AuNP surface sulfonation. Three polyelectrolyte-wrapped AuNPs with low, medium, and high concentrations of surface sulfonate groups (PSSMA 1:1, PSSMA 3:1, and PSS, respectively) were synthesized. Additionally, two small-molecule-coated AuNPs with no (4MBA) or little (4MBSA) sulfonates were synthesized. These AuNPs were introduced into the extracellular environment of THP-1 cells, and cell migration was monitored over 24 h using time-lapse brightfield microscopy. As expected, small-molecule-coated AuNPs showed no significant inhibition of chemotaxis due to limited surface sulfonates. Polyelectrolyte-wrapped AuNPs, however, demonstrated tunable control over chemotaxis inhibition, dictated by the degree of sulfonation on the AuNP surface. The fully sulfonated PSS-AuNPs had the greatest disruption of THP-1 chemotaxis and caused a significant reduction in both the FMI_x and COM_x. PSSMA-AuNPs (3:1) represented a medium level of sulfonation and subsequently caused weak inhibition of chemotaxis (significant reduction in FMI_x but not COM_x). This trend continued with the low level of sulfonation [PSSMA-AuNPs (1:1)] which caused no significant reduction in either measure of chemotaxis. Furthermore, to test whether AuNPs have a unique role in chemotaxis inhibition or if they are simply acting as molecular carriers, the effect of free polyelectrolytes on THP-1 chemotaxis was analyzed. Free PSSMA (3:1) fully eliminated any chemotactic effect from MCP-1 in solution which led to very little cell migration. Interestingly, free PSS caused a dose-dependent chemorepellent effect on THP-1 cell migration. At low concentrations, free PSS caused significant inhibition of MCP-1-induced chemotaxis. At higher concentrations, free PSS caused a full reversal in cell migration direction and acted as a

https://doi.org/10.1021/acsnanoscienceau.3c00055
ACS Nanosci. Au 2024, 4, 205−215

chemorepellent for THP-1 cells. Further work exploring the interactions of sulfated polyelectrolytes with chemokine receptors is needed to fully understand PSS chemorepulsion. While free PSS caused more profound inhibition of THP-1 chemotaxis, sulfonated AuNPs showed significant inhibition of chemotaxis as well. Leveraging the light-harnessing capabilities and biological compatibility of AuNPs coupled with better understanding of extracellular effects can enable more effective future therapeutics.

4. MATERIALS AND METHODS

4.1. Materials

Gold(III) chloride trihydrate ($HAuCl_4 \cdot 3H_2O$, ≥99.9%), hydroquinone ($C_6H_6O_2$), sodium chloride (NaCl), sodium bicarbonate ($NaHCO_3$), 4-mercaptobenzoic acid (4MBA), poly(diallyldimethylammonium chloride) (PDADMAC, MW < 100,000), poly(sodium 4-styrenesulfonate) (PSS, MW ∼70,000), and poly(4-styrenesulfonic acid-*co*-maleic acid) (PSSMA 3:1, PSSMA 1:1, MW ∼20,000) were obtained from Sigma-Aldrich. Sodium citrate tribasic dihydrate ($Na_3C_6H_5O_7 \cdot 2H_2O$) and human recombinant monocyte chemoattractant protein 1 (MCP-1) were obtained from Thermo Fisher. 4-Mercaptobenzene sulfonic acid (4MBSA, ≥95%) was obtained from BLD Pharmatech. RPMI 1640 cell culture media was prepared in house and supplemented with 10% fetal bovine serum (FBS, Sigma-Aldrich) and penicillin and streptomycin. Type I collagen (bovine, 3 mg/mL) was purchased from Advanced Biomatrix, and THP-1 were obtained from ATCC. All AuNPs were synthesized with 18 MΩ cm nanopure water in glassware cleaned with aqua regia (Caution!). Chemotaxis μ-slides were purchased from Ibidi, and image analysis was conducted using FastTrack AI software by MetaVi Laboratories.

4.2. AuNP Synthesis

Citrate-capped, 90 nm AuNPs were synthesized via a seed-mediated growth method as described previously.[52] First, gold seeds were prepared by heating 50 mL of water and 0.125 mL of 0.1 M $HAuCl_4$ to a boil. Once boiling, 1.25 mL of 1% w/v sodium citrate was added, and the solution was allowed to boil until the color changed to a deep red (∼10 min). An additional 0.25 mL of 1% w/v sodium citrate was then added, and the seeds were allowed to cool slowly to room temperature while stirring. Next, the 90 nm AuNPs were synthesized by adding 237.5 mL of water, 2.5 mL of 1% w/v $HAuCl_4$, 1.3 mL of as-synthesized seeds, 0.55 mL of 1% w/v sodium citrate, and 2.5 mL of 0.03 M hydroquinone to a 1 L flask and stirring at room temperature for 1 h. AuNPs were purified by centrifuging twice at 800*g* for 20 min. After each centrifugation, the supernatant was discarded, and pelleted AuNPs were resuspended in fresh water.

4.3. Polyelectrolyte Surface Functionalization

Purified 90 nm citrate-capped AuNPs were sequentially coated with multiple layers of polyelectrolytes using the layer-by-layer deposition method as previously described.[53] First, negatively charged citrate-AuNPs were functionalized by mixing 25 mL of AuNPs (∼0.04 nM), 5 mL of 0.01 M NaCl, and 10 mL of 10 mg/mL PDADMAC and shaking for at least 2 h. These now positively charged PDADMAC-AuNPs were purified by centrifuging twice at 800*g* as described above. Next, PDADMAC-AuNPs were subsequently functionalized with anionic polyelectrolytes [PSS, PSSMA (1:1), and PSSMA (3:1)]. Twenty-five mL of PDADMAC-AuNPs (∼0.04 nM), 5 mL of 0.01 M NaCl, and 10 mL of 10 mg/mL anionic polyelectrolyte were allowed to shake for at least 2 h followed by purification via double centrifugation. After the second centrifugation, anionic AuNPs were resuspended in ∼1 mL of water, yielding a concentrated AuNP stock solution.

4.4. Small Molecule Surface Functionalization

Small-molecule-functionalized AuNPs were synthesized via a thiol displacement reaction with the native citrate ligand. For 4MBA-AuNPs, 1.5 mg of 4MBA was dissolved in 5 mL of water and added to 25 mL of citrate-AuNPs (∼0.04 nM). For 4MBSA-AuNPs, 1.7 mg of 4MBSA was dissolved in 5 mL of water and added to 25 mL of citrate-AuNPs (∼0.04 nM). Both solutions were allowed to shake overnight and were purified via double centrifugation. Following the second centrifugation of small-molecule-functionalized AuNPs, particles were resuspended in ∼1 mL of water.

4.5. AuNP Characterization

Gold nanoparticles were characterized by ultraviolet−visible spectroscopy (UV−vis), ζ-potential spectroscopy, dynamic light scattering (DLS), and transmission electron microscopy (TEM). UV−vis was used to qualitatively check the diameter of AuNPs as evidenced by a surface plasmon maximum of around 558 nm. Colloidal stability was also assessed via UV−vis by observing the lack of excessive peak broadening and the lack of appreciable absorbance above 800 nm. A negative ζ-potential was used to confirm the presence of citrate on the AuNP surface. DLS was used to determine the AuNP hydrodynamic diameter (98.7 ± 0.4 nm) in solution; TEM was used to quantify the AuNP core diameter (92 ± 11 nm). ζ-Potential was also used to characterize AuNP surface functionalization. The success of polyelectrolyte surface functionalization was monitored by observing a characteristic flip in ζ-potential from negative to positive to negative for the anionic, cationic, and anionic layers, respectively.

Small-molecule functionalization was confirmed with surface-enhanced Raman spectroscopy by monitoring the presence of characteristic ligand peaks. Samples were prepared by drop-casting 2 μL of concentrated AuNP solutions (∼0.5 nM) onto a glass microscope slide and allowed to dry completely. This process was repeated 5−10 times to deposit enough sample for a clean spectrum. Samples were irradiated with a 785 nm laser with an integration time of 100 μs and three spectral coadditions.

The stability of all functionalized AuNPs in RPMI cell media was assessed with UV−vis. AuNPs were first incubated in a solution of 20% fetal bovine serum (FBS) in water overnight. To this solution, 2× RPMI was added to yield 0.04 nM AuNPs in RPMI with 10% FBS. This solution was allowed to incubate 24 h to simulate a full chemotaxis assay before UV−vis spectra were recorded to confirm long-term colloidal stability in cell media.

4.6. Degree of Sulfonation Determination

AuNP solutions (0.04 nM) were adjusted to pH 3 with HCl. At pH 3, all carboxylic acid groups on the AuNPs will be fully protonated, eliminating their contribution to electrostatic colloidal stability. 100 μL of AuNP solution was added to separate wells on a 96-well plate. To this was added 10 μL of increasing concentrations (0−0.35 M) of NaCl for a final concentration of 0−0.032 M NaCl, 0.036 nM AuNPs. The plate was allowed to shake gently for 20 min prior to absorbance being read at 560 nm on a plate reader. By monitoring aggregation (measured by a reduction in absorbance at 560 nm) at increasing ionic strengths, the relative sulfonate concentration on AuNP surfaces can be determined. Extinction measurements were normalized to the AuNP absorbance without NaCl addition.

4.7. Cell Culture

Human monocytic cell line THP-1 was cultured at densities of up to 1.5×10^6 cells/mL in a 75 cm^2 cell culture flask. THP-1 cells were grown in 1640 RPMI cell media containing 10% FBS, 2 mM L-glutamine, and 1% penicillin−streptomycin. Cell media was changed every 2−3 days. Cells were grown until the total cell count was near 20 million cells at which they were used for chemotaxis assays. Cells were used for chemotaxis assays between passage 10 and passage 18. Cells were counted and monitored for any phenotypic changes using an optical microscope and hemocytometer.

4.8. Chemotaxis Assay

Chemotaxis assays were conducted using the chemotaxis μ-slide from Ibidi following manufacturer protocol. Initially, the μ-slide and cell media were preincubated overnight at 37 °C and 5% CO_2. All AuNPs were also preincubated in 20% FBS overnight prior to use in chemotaxis assays to ensure colloidal stability when they were introduced to cell media. Next, THP-1 cells were seeded at a density

https://doi.org/10.1021/acsnanoscienceau.3c00055
ACS Nanosci. Au 2024, 4, 205−215

of 3×10^6 cells/mL in a 1.5 mg/mL type I collagen matrix by mixing 20 μL of 10× MEM, 20 μL of water, 10 μL of 7.5% sodium bicarbonate, 50 μL of RPMI, 150 μL of 3 mg/mL collagen, and 50 μL of 18×10^6 cells/mL THP-1. The collagen matrix solution was then added to the chemotaxis μ-slide and allowed to solidify at 37 °C and 5% CO_2 for 45 min. Following collagen gelation, the exposure reservoirs were filled with the solutions of interest. For the positive control, one reservoir was filled with 50 ng/mL MCP-1 in RPMI, while the other was filled with RPMI alone. For the negative control, both reservoirs were filled with RPMI, and for the balanced MCP-1 control, both reservoirs were filled with 25 ng/mL MCP-1 in RPMI. For AuNP exposure conditions, one reservoir was filled with RPMI, and the other was filled with 50 ng/mL MCP-1, 0.02 nM AuNPs in RPMI. AuNP controls were also conducted with 0.02 nM AuNPs in RPMI in one reservoir and RPMI in the other to ensure AuNPs alone have no impact on chemotaxis. Free polyelectrolyte controls were conducted by adding 0.2 mg/mL polyelectrolyte and 50 ng/mL MCP-1 in RPMI to one reservoir and adding RPMI to the other reservoir. Finally, the dose-dependent response of free PSS was conducted by adding 0−0.20 mg/mL PSS, 50 ng/mL MCP-1 in RPMI to one reservoir, and RPMI to the other reservoir.

Cell migration was monitored via bright-field microscopy on a Zeiss Axio Z1 Observer microscope. Timelapse images were taken every 10 min for 24 h to monitor cell movement while being kept at 37 °C and 5% CO_2.

4.9. Statistical Analysis

Timelapse images were analyzed using FastTrack AI by MetaVi Laboratories. Cells that moved at least 100 μm and were recognized by the software for more than 12 of the 24 h were included in further analysis. A given experiment was considered an appropriate replicate if five or more cells were tracked by FastTrack AI (range: n = 5−85; average: n = 24). All conditions tested consist of at least six replicates that were collected on at least three separate days to ensure reliability of results. The Dunnett's multiple comparison test was used to determine if a given experimental condition was significantly different from the positive control ($p < 0.05$ was considered statistically significant). Statistical analysis and figure plotting was conducted in GraphPad Prism 6.0c.

4.10. Instrumentation

Absorption spectra were recorded on a Cary 500 scan UV−vis near-IR spectrophotometer (Agilent Technologies). Zeta potential measurements were taken on Malvern Zetasizer Nano ZS. Transmission electron microscopy images were taken on a JEOL 2100 cryo electron microscope (200 kV). SERS spectra were recorded on a B&W Tek i-Raman Plus. Time-lapse bright-field microscopy was conducted on a Zeiss Axio Observer Z1 inverted microscope with an incubation chamber, CO_2 sensor, and heated stage. AuNP absorption for the sulfonate concentration experiment was conducted on a SpectraMax M2 plate reader (Molecular Devices).

■ ASSOCIATED CONTENT

Supporting Information

The Supporting Information is available free of charge at https://pubs.acs.org/doi/10.1021/acsnanoscienceau.3c00055.

Analysis of cell migration perpendicular to the chemoattractant gradient and representative cell trajectory plots and Rayleigh tests (PDF)

Time-lapse video of the positive control (MP4)

Time-lapse video of the negative control (MP4)

■ AUTHOR INFORMATION

Corresponding Author

Catherine J. Murphy − *Department of Chemistry, University of Illinois Urbana-Champaign, Urbana, Illinois 61801, United States;* orcid.org/0000-0001-7066-5575; Email: murphycj@illinois.edu

Author

Maxwell G. Tetrick − *Department of Chemistry, University of Illinois Urbana-Champaign, Urbana, Illinois 61801, United States*

Complete contact information is available at: https://pubs.acs.org/10.1021/acsnanoscienceau.3c00055

Notes

The authors declare no competing financial interest.

■ ACKNOWLEDGMENTS

We thank the National Institutes of Health (5R01-GM12845) for their support. This material is based upon work supported by the National Science Foundation Graduate Research Fellowship under Grant no. DGE 21-46756 to M.G.T. We thank Dr. Bashar Emon for his help with mechanical stiffness measurements. We thank Dr. Sandy McMasters from the UIUC Cell Media Facility for her assistance with cell culture.

■ REFERENCES

(1) Murphy, C. J.; Vartanian, A. M.; Geiger, F. M.; Hamers, R. J.; Pedersen, J.; Cui, Q.; Haynes, C. L.; Carlson, E. E.; Hernandez, R.; Klaper, R. D.; Orr, G.; Rosenzweig, Z. Biological Responses to Engineered Nanomaterials: Needs for the next Decade. *ACS Cent. Sci.* **2015**, *1* (3), 117−123.

(2) Zhu, M.; Nie, G.; Meng, H.; Xia, T.; Nel, A.; Zhao, Y. Physicochemical Properties Determine Nanomaterial Cellular Uptake, Transport, and Fate. *Acc. Chem. Res.* **2013**, *46* (3), 622−631.

(3) Hu, X.; Zhang, Y.; Ding, T.; Liu, J.; Zhao, H. Multifunctional Gold Nanoparticles: A Novel Nanomaterial for Various Medical Applications and Biological Activities. *Front. Bioeng. Biotechnol.* **2020**, *8* (990), 1−17.

(4) Jeong, H. H.; Choi, E.; Ellis, E.; Lee, T. C. Recent Advances in Gold Nanoparticles for Biomedical Applications: From Hybrid Structures to Multi-Functionality. *J. Mater. Chem. B* **2019**, *7*, 3480−3496.

(5) Alkilany, A. M.; Rachid, O.; Alkawareek, M. Y.; Billa, N.; Daou, A.; Murphy, C. J. PLGA-Gold Nanocomposite: Preparation and Biomedical Applications. *Pharmaceutics* **2022**, *14*, 660.

(6) Murphy, C. J.; Chang, H. H.; Falagan-Lotsch, P.; Gole, M. T.; Hofmann, D. M.; Hoang, K. N. L.; McClain, S. M.; Meyer, S. M.; Turner, J. G.; Unnikrishnan, M.; Wu, M.; Zhang, X.; Zhang, Y. Virus-Sized Gold Nanorods: Plasmonic Particles for Biology. *Acc. Chem. Res.* **2019**, *52* (8), 2124−2135.

(7) Drozdick, H. K.; Weiss, R.; Sullivan, C. M.; Wieghold, S.; Nienhaus, L. Widespread Opportunities for Materials Engineering of Nanocrystals: Synthetically Tailorable Effects and Methodologies. *Matter* **2022**, *5*, 1645−1669.

(8) Mitchell, M. J.; Billingsley, M. M.; Haley, R. M.; Wechsler, M. E.; Peppas, N. A.; Langer, R. Engineering Precision Nanoparticles for Drug Delivery. *Nat. Rev. Drug Discovery* **2021**, *20*, 101−124.

(9) Smith, B. R.; Gambhir, S. S. Nanomaterials for in Vivo Imaging. *Chem. Rev.* **2017**, *117* (3), 901−986.

(10) Bogart, L. K.; Pourroy, G.; Murphy, C. J.; Puntes, V.; Pellegrino, T.; Rosenblum, D.; Peer, D.; Lévy, R. Nanoparticles for Imaging, Sensing, and Therapeutic Intervention. *ACS Nano* **2014**, *8* (4), 3107−3122.

(11) Rastinehad, A. R.; Anastos, H.; Wajswol, E.; Winoker, J. S.; Sfakianos, J. P.; Doppalapudi, S. K.; Carrick, M. R.; Knauer, C. J.; Taouli, B.; Lewis, S. C.; Tewari, A. K.; Schwartz, J. A.; Canfield, S. E.; George, A. K.; West, J. L.; Halas, N. J. Gold Nanoshell-Localized Photothermal Ablation of Prostate Tumors in a Clinical Pilot Device Study. *Proc. Natl. Acad. Sci. U.S.A.* **2019**, *116* (37), 18590−18596.

(12) Lee, E.; Lee, M.; Kwon, S.; Kim, J.; Kwon, Y. Systematic and Mechanistic Analysis of AuNP-Induced Nanotoxicity for Risk Assessment of Nanomedicine. *Nano Convergence* **2022**, *9*, 27.
(13) Abtahi, S. M. H.; Trevisan, R.; Di Giulio, R.; Murphy, C. J.; Saleh, N. B.; Vikesland, P. J. Implications of Aspect Ratio on the Uptake and Nanotoxicity of Gold Nanomaterials. *NanoImpact* **2019**, *14*, 100153.
(14) Chen, Y. Y.; Syed, A. M.; MacMillan, P.; Rocheleau, J. V.; Chan, W. C. W. Flow Rate Affects Nanoparticle Uptake into Endothelial Cells. *Adv. Mater.* **2020**, *32*, 1906274.
(15) Yang, J. A.; Phan, H. T.; Vaidya, S.; Murphy, C. J. Nanovacuums: Nanoparticle Uptake and Differential Cellular Migration on a Carpet of Nanoparticles. *Nano Lett.* **2013**, *13* (5), 2295−2302.
(16) Kumar, Y.; Sinha, A. S. K.; Nigam, K. D. P.; Dwivedi, D.; Sangwai, J. S. Functionalized Nanoparticles: Tailoring Properties through Surface Energetics and Coordination Chemistry for Advanced Biomedical Applications. *Nanoscale* **2023**, *15*, 6075−6104.
(17) Qiu, Y.; Liu, Y.; Wang, L.; Xu, L.; Bai, R.; Ji, Y.; Wu, X.; Zhao, Y.; Li, Y.; Chen, C. Surface Chemistry and Aspect Ratio Mediated Cellular Uptake of Au Nanorods. *Biomaterials* **2010**, *31*, 7606−7619.
(18) Zhang, J.; Mou, L.; Jiang, X. Surface Chemistry of Gold Nanoparticles for Health-Related Applications. *Chem. Sci.* **2020**, *11*, 923−936.
(19) Alkilany, A. M.; Nagaria, P. K.; Hexel, C. R.; Shaw, T. J.; Murphy, C. J.; Wyatt, M. D. Cellular Uptake and Cytotoxicity of Gold Nanorods: Molecular Origin of Cytotoxicity and Surface Effects. *Small* **2009**, *5* (6), 701−708.
(20) Falagan-Lotsch, P.; Grzincic, E. M.; Murphy, C. J. One Low-Dose Exposure of Gold Nanoparticles Induces Long-Term Changes in Human Cells. *Proc. Natl. Acad. Sci. U.S.A.* **2016**, *113* (47), 13318−13323.
(21) Nunes, Á. M.; Falagan-Lotsch, P.; Roslend, A.; Meneghetti, M. R.; Murphy, C. J. Cytotoxicity of Mini Gold Nanorods: Intersection with Extracellular Vesicles. *Nanoscale Adv.* **2023**, *5* (3), 733−741.
(22) Melby, E. S.; Lohse, S. E.; Park, J. E.; Vartanian, A. M.; Putans, R. A.; Abbott, H. B.; Hamers, R. J.; Murphy, C. J.; Pedersen, J. A. Cascading Effects of Nanoparticle Coatings: Surface Functionalization Dictates the Assemblage of Complexed Proteins and Subsequent Interaction with Model Cell Membranes. *ACS Nano* **2017**, *11* (6), 5489−5499.
(23) Nienhaus, K.; Nienhaus, G. U. Mechanistic Understanding of Protein Corona Formation around Nanoparticles: Old Puzzles and New Insights. *Small* **2023**, *19*, 2301663.
(24) Park, S.; Ha, M. K.; Lee, Y.; Song, J.; Yoon, T. H. Effects of Immune Cell Heterogeneity and Protein Corona on the Cellular Association and Cytotoxicity of Gold Nanoparticles: A Single-Cell-Based, High-Dimensional Mass Cytometry Study. *ACS Nanosci. Au* **2023**, *3* (4), 323−334.
(25) Mahl, D.; Greulich, C.; Meyer-Zaika, W.; Köller, M.; Epple, M. Gold Nanoparticles: Dispersibility in Biological Media and Cell-Biological Effect. *J. Mater. Chem.* **2010**, *20* (29), 6176−6181.
(26) Wheeler, K. E.; Chetwynd, A. J.; Fahy, K. M.; Hong, B. S.; Tochihuitl, J. A.; Foster, L. A.; Lynch, I. Environmental Dimensions of the Protein Corona. *Nat. Nanotechnol.* **2021**, *16* (6), 617−629.
(27) Grzincic, E. M.; Murphy, C. J. Gold Nanorods Indirectly Promote Migration of Metastatic Human Breast Cancer Cells in Three-Dimensional Cultures. *ACS Nano* **2015**, *9* (7), 6801−6816.
(28) Maksoudian, C.; Izci, M.; Salembier, R.; Gilabert, I. P.; Gonçalves, F. R.; Luci, C. R.; Bolea-Fernandez, E.; Vanhaecke, F.; Manshian, B. B.; Soenen, S. J. Gold Nanoparticle Delivery to Solid Tumors by Macrophage Depletion, Hypoxia Inhibition, and Collagen Degradation. *ACS Appl. Nano Mater.* **2023**, *6* (9), 7605−7618.
(29) Zhang, Y.; Elechalawar, C. K.; Hossen, M. N.; Francek, E. R.; Dey, A.; Wilhelm, S.; Bhattacharya, R.; Mukherjee, P. Gold Nanoparticles Inhibit Activation of Cancer-Associated Fibroblasts by Disrupting Communication from Tumor and Microenvironmental Cells. *Bioact. Mater.* **2021**, *6*, 326−332.
(30) Zhang, Y.; Xiong, X.; Huai, Y.; Dey, A.; Hossen, M. N.; Roy, R. V.; Elechalawar, C. K.; Rao, G.; Bhattacharya, R.; Mukherjee, P. Gold Nanoparticles Disrupt Tumor Microenvironment - Endothelial Cell Cross Talk to Inhibit Angiogenic Phenotypes in Vitro. *Bioconjugate Chem.* **2019**, *30* (6), 1724−1733.
(31) Luo, J.; Walker, M.; Xiao, Y.; Donnelly, H.; Dalby, M. J.; Salmeron-Sanchez, M. The Influence of Nanotopography on Cell Behaviour through Interactions with the Extracellular Matrix - A Review. *Bioact. Mater.* **2022**, *15*, 145−159.
(32) Wang, L.; Dou, J.; Jiang, W.; Wang, Q.; Liu, Y.; Liu, H.; Wang, Y. Enhanced Intracellular Transcytosis of Nanoparticles by Degrading Extracellular Matrix for Deep Tissue Radiotherapy of Pancreatic Adenocarcinoma. *Nano Lett.* **2022**, *22* (17), 6877−6887.
(33) Wilson, C. G.; Sisco, P. N.; Goldsmith, E. C.; Murphy, C. J. Glycosaminoglycan-Functionalized Gold Nanorods: Interactions with Cardiac Cells and Type I Collagen. *J. Mater. Chem.* **2009**, *19* (35), 6332−6340.
(34) Auría-Soro, C.; Nesma, T.; Juanes-Velasco, P.; Landeira-Viñuela, A.; Fidalgo-Gomez, H.; Acebes-Fernandez, V.; Gongora, R.; Almendral Parra, M. J.; Manzano-Roman, R.; Fuentes, M. Interactions of Nanoparticles and Biosystems: Microenvironment of Nanoparticles and Biomolecules in Nanomedicine. *Nanomaterials* **2019**, *9*, 1365.
(35) Levine, H.; Rappel, W. J. The Physics of Eukaryotic Chemotaxis. *Phys. Today* **2013**, *66* (2), 24−30.
(36) Jin, T.; Xu, X.; Hereld, D. Chemotaxis, Chemokine Receptors and Human Disease. *Cytokines* **2008**, *44*, 1−8.
(37) Song, L.; Nadkarni, S. M.; Bödeker, H. U.; Beta, C.; Bae, A.; Franck, C.; Rappel, W. J.; Loomis, W. F.; Bodenschatz, E. Dictyostelium Discoideum Chemotaxis: Threshold for Directed Motion. *Eur. J. Cell Biol.* **2006**, *85* (9−10), 981−989.
(38) Friedl, P.; Wolf, K. Plasticity of Cell Migration: A Multiscale Tuning Model. *J. Cell Biol.* **2010**, *188*, 11−19.
(39) Roussos, E. T.; Condeelis, J. S.; Patsialou, A. Chemotaxis in Cancer. *Nat. Rev. Cancer* **2011**, *11*, 573−587.
(40) Friedrich, B. M.; Jülicher, F. Chemotaxis of Sperm Cells. *Proc. Natl. Acad. Sci. U.S.A.* **2007**, *104* (33), 13256−13261.
(41) Biasci, D.; Smoragiewicz, M.; Connell, C. M.; Wang, Z.; Gao, Y.; Thaventhiran, J. E. D.; Basu, B.; Magiera, L.; Johnson, T. I.; Bax, L.; Gopinathan, A.; Isherwood, C.; Gallagher, F. A.; Pawula, M.; Hudecova, I.; Gale, D.; Rosenfeld, N.; Barmpounakis, P.; Popa, E. C.; Brais, R.; Godfrey, E.; Mir, F.; Richards, F. M.; Fearon, D. T.; Janowitz, T.; Jodrell, D. I. CXCR4 Inhibition in Human Pancreatic and Colorectal Cancers Induces an Integrated Immune Response. *Proc. Natl. Acad. Sci. U.S.A.* **2020**, *117* (46), 28960−28970.
(42) Cabrini, G.; Rimessi, A.; Borgatti, M.; Lampronti, I.; Finotti, A.; Pinton, P.; Gambari, R. Role of Cystic Fibrosis Bronchial Epithelium in Neutrophil Chemotaxis. *Front. Immunol.* **2020**, *11* (1438), 1−17.
(43) Zhang, X.; Falagan-Lotsch, P.; Murphy, C. J. Nanoparticles Interfere with Chemotaxis: An Example of Nanoparticles as Molecular "Knockouts" at the Cellular Level. *ACS Nano* **2021**, *15* (5), 8813−8825.
(44) Deshmane, S. L.; Kremlev, S.; Amini, S.; Sawaya, B. E. Monocyte Chemoattractant Protein-1 (MCP-1): An Overview. *J. Interferon Cytokine Res.* **2009**, *29*, 313−326.
(45) Schneider, I. C.; Haugh, J. M. Mechanisms of Gradient Sensing and Chemotaxis: Conserved Pathways, Diverse Regulation. *Cell Cycle* **2006**, *5* (11), 1130−1134.
(46) Melvin, A. T.; Welf, E. S.; Wang, Y.; Irvine, D. J.; Haugh, J. M. In Chemotaxing Fibroblasts, Both High-Fidelity and Weakly Biased Cell Movements Track the Localization of PI3K Signaling. *Biophys. J.* **2011**, *100* (8), 1893−1901.
(47) Wang, Y.; Irvine, D. J. Convolution of Chemoattractant Secretion Rate, Source Density, and Receptor Desensitization Direct Diverse Migration Patterns in Leukocytes. *Integr. Biol.* **2013**, *5* (3), 481−494.
(48) Wu, D. Signaling Mechanisms for Regulation of Chemotaxis. *Cell Res.* **2005**, *15* (1), 52−56.

https://doi.org/10.1021/acsnanoscienceau.3c00055
ACS Nanosci. Au 2024, 4, 205−215

(49) Ludeman, J. P.; Stone, M. J. The Structural Role of Receptor Tyrosine Sulfation in Chemokine Recognition. *Br. J. Pharmacol.* **2014**, *171*, 1167−1179.
(50) Tan, J. H. Y.; Ludeman, J. P.; Wedderburn, J.; Canals, M.; Hall, P.; Butler, S. J.; Taleski, D.; Christopoulos, A.; Hickey, M. J.; Payne, R. J.; Stone, M. J. Tyrosine Sulfation of Chemokine Receptor CCR2 Enhances Interactions with Both Monomeric and Dimeric Forms of the Chemokine Monocyte Chemoattractant Protein-1 (MCP-1). *J. Biol. Chem.* **2013**, *288* (14), 10024−10034.
(51) Stone, M. J.; Payne, R. J. Homogeneous Sulfopeptides and Sulfoproteins: Synthetic Approaches and Applications To Characterize the Effects of Tyrosine Sulfation on Biochemical Function. *Acc. Chem. Res.* **2015**, *48* (8), 2251−2261.
(52) Perrault, S. D.; Chan, W. C. W. Synthesis and Surface Modification of Highly Monodispersed, Spherical Gold Nanoparticles of 50−200 Nm. *J. Am. Chem. Soc.* **2009**, *131* (47), 17042−17043.
(53) Gole, A.; Murphy, C. J. Polyelectrolyte-Coated Gold Nanorods: Synthesis, Characterization and Immobilization. *Chem. Mater.* **2005**, *17* (6), 1325−1330.
(54) Foxman, E. F.; Kunkel, E. J.; Butcher, E. C. Integrating Conflicting Chemotactic Signals: The Role of Memory in Leukocyte Navigation. *J. Cell Biol.* **1999**, *147* (3), 577−588.
(55) μ-Slide Chemotaxis. https://ibidi.com/channel-slides/9-slide-chemotaxis-ibitreat.html (accessed 2024-01−28).
(56) Wilson, C. G.; Sisco, P. N.; Gadala-Maria, F. A.; Murphy, C. J.; Goldsmith, E. C. Polyelectrolyte-Coated Gold Nanorods and Their Interactions with Type I Collagen. *Biomaterials* **2009**, *30* (29), 5639−5648.
(57) Li, Z.; Greden, K.; Alvarez, P. J. J.; Gregory, K. B.; Lowry, G. V. Adsorbed Polymer and NOM Limits Adhesion and Toxicity of Nano Scale Zerovalent Iron to E. Coli. *Environ. Sci. Technol.* **2010**, *44* (9), 3462−3467.
(58) Hauck, T. S.; Ghazani, A. A.; Chan, W. C. W. Assessing the Effect of Surface Chemistry on Gold Nanorod Uptake, Toxicity, and Gene Expression in Mammalian Cells. *Small* **2008**, *4* (1), 153−159.
(59) Pitchaimani, A.; Nguyen, T. D. T.; Koirala, M.; Zhang, Y.; Aryal, S. Impact of Cell Adhesion and Migration on Nanoparticle Uptake and Cellular Toxicity. *Toxicol. in Vitro* **2017**, *43*, 29−39.
(60) Proudfoot, A. E. I.; Handel, T. M.; Johnson, Z.; Lau, E. K.; LiWang, P.; Clark-Lewis, I.; Borlat, F.; Wells, T. N. C.; Kosco-Vilbois, M. H. Glycosaminoglycan Binding and Oligomerization Are Essential for the in Vivo Activity of Certain Chemokines. *Proc. Natl. Acad. Sci. U.S.A.* **2003**, *100* (4), 1885−1890.
(61) Chhabra, M.; Doherty, G. G.; See, N. W.; Gandhi, N. S.; Ferro, V. From Cancer to COVID-19: A Perspective on Targeting Heparan Sulfate-Protein Interactions. *Chem. Rec.* **2021**, *21*, 3087−3101.
(62) Perez, S.; Makshakova, O.; Angulo, J.; Bedini, E.; Bisio, A.; de Paz, J. L.; Fadda, E.; Guerrini, M.; Hricovini, M.; Hricovini, M.; Lisacek, F.; Nieto, P. M.; Pagel, K.; Paiardi, G.; Richter, R.; Samsonov, S. A.; Vivès, R. R.; Nikitovic, D.; Ricard Blum, S. Glycosaminoglycans: What Remains To Be Deciphered? *JACS Au* **2023**, *3*, 628−656.
(63) Farrugia, B. L.; Lord, M. S.; Melrose, J.; Whitelock, J. M. The Role of Heparan Sulfate in Inflammation, and the Development of Biomimetics as Anti-Inflammatory Strategies. *J. Histochem. Cytochem.* **2018**, *66*, 321−336.
(64) Shanthamurthy, C. D.; Leviatan Ben-Arye, S.; Kumar, N. V.; Yehuda, S.; Amon, R.; Woods, R. J.; Padler-Karavani, V.; Kikkeri, R. Heparan Sulfate Mimetics Differentially Affect Homologous Chemokines and Attenuate Cancer Development. *J. Med. Chem.* **2021**, *64* (6), 3367−3380.
(65) Jain, P.; Shanthamurthy, C. D.; Leviatan Ben-Arye, S.; Woods, R. J.; Kikkeri, R.; Padler-Karavani, V. Discovery of Rare Sulfated: N -Unsubstituted Glucosamine Based Heparan Sulfate Analogs Selectively Activating Chemokines. *Chem. Sci.* **2021**, *12* (10), 3674−3681.
(66) Hsiao, P. Y.; Luijten, E. Salt-Induced Collapse and Reexpansion of Highly Charged Flexible Polyelectrolytes. *Phys. Rev. Lett.* **2006**, *97* (14), 148301.
(67) Stoll, S.; Chodanowski, P. Polyelectrolyte Adsorption on an Oppositely Charged Spherical Particle. Chain Rigidity Effects. *Macromolecules* **2002**, *35* (25), 9556−9562.
(68) Carnal, F.; Stoll, S. Adsorption of Weak Polyelectrolytes on Charged Nanoparticles. Impact of Salt Valency, PH, and Nanoparticle Charge Density. Monte Carlo Simulations. *J. Phys. Chem. B* **2011**, *115* (42), 12007−12018.
(69) Voigt, J.; Christensen, J.; Shastri, V. P. Differential Uptake of Nanoparticles by Endothelial Cells through Polyelectrolytes with Affinity for Caveolae. *Proc. Natl. Acad. Sci. U.S.A.* **2014**, *111* (8), 2942−2947.
(70) Lin, A. Y.; Lunsford, J.; Bear, A. S.; Young, J. K.; Eckels, P.; Luo, L.; Foster, A. E.; Drezek, R. A. High-Density Sub-100-Nm Peptide-Gold Complexes Improve Vaccine by Dendritic Cells in Vitro. *Nanoscale Res. Lett.* **2013**, *8*, 72.

https://doi.org/10.1021/acsnanoscienceau.3c00055
ACS Nanosci. Au 2024, 4, 205−215